ACS APPLIED NANO MATERIALS

www.acsanm.org

Article

2D in-Plane Ordered MXene Nanosheets Derived from $(Mo_{2/3}Er_{1/3})_2AlC$ Rare-Earth i-MAX for Energy Storage Applications

Nisha Hiralal Makani, Chandra M. Adhikari, Shanna Marie M. Alonzo, Bishnu Prasad Bastakoti, Binod K. Rai, and Bhoj Raj Gautam*

Cite This: *ACS Appl. Nano Mater.* 2026, 9, 1089−1098

Read Online

ACCESS | Metrics & More | Article Recommendations | Supporting Information

ABSTRACT: MXenes have become one of the most versatile families of two-dimensional (2D) materials due to their high conductivity, hydrophilicity, and remarkable electrochemical performance. This has stimulated intense efforts to design and synthesize MXenes, including structurally unique in-plane ordered 2D MXenes called i-MXenes. Here, we have synthesized the quaternary rare earth (RE)-based i-MAX phase $(Mo_{2/3}Er_{1/3})_2AlC$ using an arc melting method, and the corresponding 2D i-MXene was then obtained through a LiF/HCl soft etching process. Literature studies have shown that Al and the RE element are etched out during the etching process, leading to the formation of pure vacancy-ordered $Mo_{1.33}C$ 2D i-MXene. However, our investigation reveals that upon exposure to a fluorine solution, the i-MAX phase forms RE fluoride impurities, which are challenging to remove through HCl−DI water washing and persist in the final product, resulting in impure $Mo_{1.33}C$@Er i-MXene. These results were confirmed by various characterizations such as X-ray diffraction, Raman spectroscopy, X-ray photoelectron spectroscopy, and scanning transmission electron microscopy. Although the $Mo_{1.33}C$@Er electrode showed a 24-fold increase in specific capacitance compared to its parent i-MAX phase, it still exhibited a high charge-transfer resistance arising from the insulating nature of RE fluoride byproducts, which adversely influence the overall capacitance behavior of the synthesized 2D $Mo_{1.33}C$@Er i-MXenes. This study contributes to identifying pathways for the preparation of pure 2D i-MXenes from RE-based i-MAX phases and developing improved synthesis methods. With additional process optimization, the 2D i-MXene holds a strong potential for electrochemical energy storage applications. Additionally, the electronic structures of $Mo_{1.33}C$ were theoretically studied using first-principles density functional theory calculations, which revealed that pristine $Mo_{1.33}C$ is metallic, and this metallic nature is preserved even with −O, −F, and mixed functionalization.

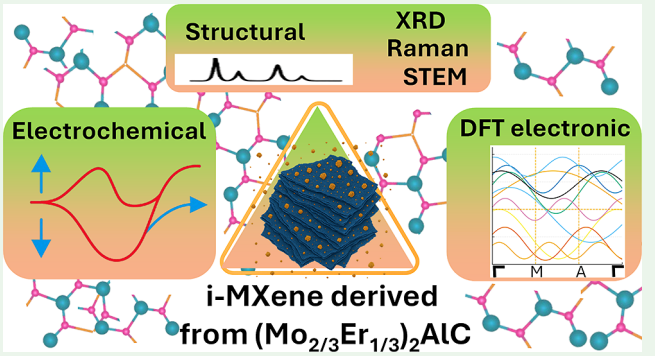

KEYWORDS: *i-MAX, i-MXenes, rare earth, vacancy, structural, electrochemical, electronic*

1. INTRODUCTION

In 2024, the International Union of Pure and Applied Chemistry recognized two-dimensional (2D) MXenes in its Top Ten Emerging Technologies in Chemistry, underscoring their significance in advancing chemical sciences,[1] which highlights that MXenes are widely researched materials with a broad range of applications, particularly in areas such as energy storage field due to their exceptional conductivity and chemical stability.[2−6] MXenes are 2D transition-metal carbides or nitrides produced by etching the A element from MAX phases.[3,7,8] MAX phases are layered ternary phases with the general formula $M_{n+1}AX_n$ (where M is an early transition metal, A is an element from groups 13−14, and X is carbon and/or nitrogen).[9,10] The etching process, commonly carried out using fluoride-containing solutions such as HF or LiF/HCl, removes the A layer while preserving the M−X slabs, yielding 2D sheets with surface terminations (Tx = −F, −O, −OH).[7,11,12] Therefore, the general formula for MXenes is given by $M_{n+1}X_nT_x$. The first 2D MXene, $Ti_3C_2T_x$, was reported in 2011 and synthesized from the Ti_3AlC_2 MAX phase by etching the Al.[13] Subsequently, several MAX phases with single transition metals, such as Nb_2AlC, V_2AlC, and $Ti_3Al(CN)$, were developed, along with their corresponding MXenes.[14−18] In 2015, MAX phases featuring double transition metals with ordered structures were reported, such as $Mo_2Ti_2AlC_3$ and Cr_2TiAlC_2.[19] These structures consist of one or two metal layers sandwiched between two transition metal layers and were termed out-of-plane ordered (o-MAX) phases, with their corresponding MXenes named o-MXenes.[20] Over the years,

Received: October 17, 2025
Revised: December 22, 2025
Accepted: December 23, 2025
Published: January 6, 2026

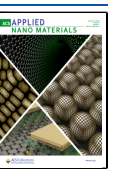

research on MAX phases has rapidly progressed in the pursuit of novel MXenes. In 2017, a new family of in-plane ordered MAX phases, known as i-MAX phases, was introduced.[21] These quaternary MAX phases follow the general formula $(M_{2/3}'M_{1/3}'')_2AX$, where M′ and M″ can include elements such as Sc, Y, Zr, Hf, V, Cr, Mo, Mn, and W in a 2:1 ratio.[22−31] The A element is either Al or Ga, while X is C. Additionally, i-MAX phases were synthesized utilizing rare-earth (RE) elements, including Gd, Tb, Dy, Ho, Er, Y, Tm, Yb, and Lu.[24,32−36] In the i-MAX phase, M′ atoms form a honeycomb lattice, while M″ atoms fill the centers of the hexagons. The extrusion of M″ atoms from the M′ layers toward the A layer results in a Kagome lattice in either a monoclinic lattice structure (space group *C*2/*c*, *C*2/*m*) or an orthorhombic lattice structure (space group *Cmcm*).[21,33,37]

The first i-MAX phase synthesized was $(Mo_{2/3}Sc_{1/3})_2AlC$, and from this, the first 2D i-MXene was derived.[21] This process led to the discovery of novel vacancy-ordered $Mo_{1.33}C$ 2D i-MXenes, as both Al and Sc were etched during the etching process. Subsequent electrochemical measurements revealed exceptionally low resistivity and high capacitance values.[21] Moreover, asymmetric supercapacitors constructed from 2D i-MXene ($Mo_{1.33}C//Mn_xO_n$) exhibit outstanding cycling stability;[38] building on these studies, new 2D i-MXenes $W_{1.33}C$ were developed.[39−41] Meshkian et al.[41] presented a combined theoretical and experimental study on the structural investigation of vacancy-ordered 2D i-MXene, demonstrating that $W_{1.33}C$ synthesized from two different parent materials (such as $(W_{2/3}Sc_{1/3})_2AlC$ and $(W_{2/3}Y_{1/3})_2AlC$) exhibits distinct surface functional groups, which are known to significantly influence their fundamental properties.[41] Persson et al.[42] studied the selective etching of the M″ and A elements, demonstrating that by adjusting the etchant concentration, selective etching can be achieved, leading to different compositions of 2D i-MXenes.[42] Additionally, 2D i-MXenes $Mo_{1.33}C$ and $W_{1.33}C$ were synthesized from rare earth (RE)-based i-MAX phases, and their electrochemical performance was thoroughly examined.[43,44] The capacitance of $Mo_{1.33}C$, derived from $(Mo_{2/3}RE_{1/3})_2AlC$, varied depending on the specific RE element used.[44] Furthermore, Chen et al.[45] synthesized $(W_{2/3}Mo_{2/3})C$ 2D i-MXene from the solid solution $(W_{1/3}Mo_{1/3}RE_{1/3})_2AlC$ i-MAX phase, and a specific capacitance of 120 F/g at 1 A/g was obtained. It was further treated with hydrazine monohydrate ($N_2H_4{\cdot}H_2O$) and rGO, which resulted in an increase in specific capacitance due to the presence of more O-/N-containing surface terminations and the formation of an interactive microstructure that improved the overall conductivity of the electrode.[45,46] In addition to experimental investigations, several theoretical studies have also been carried out on 2D i-MXenes. Mostafaei et al.[47,48] examined the electronic structure and optical properties of $((Mo/W)_{2/3}(Sc/Y)_{1/3})_2CO_2$ 2D i-MXenes, and Khazaei et al.[49] focused on the electronic structure of functionalized 2D $(Mo_{2/3}Y_{1/3})_2C$. These works revealed that O-functionalized i-MXenes exhibit semiconducting behavior, whereas F-functionalized counterparts are metallic in nature.[50]

As mentioned in the above studies, during the synthesis of 2D i-MXenes from the quaternary i-MAX phase, M″ (Sc, Y, and RE) elements can also be etched out by reacting with fluoride ions, forming byproducts, similar to the reaction between A elements and fluorides.[21,43,44] In conventional MAX phases, the A elements, usually aluminum, react with fluoride to form AlF_3, which easily dissolves in HCl and deionized (DI) water, facilitating its removal. This process can be likened to separating a mixture of rock and salt, where the "rock" represents the MXene and the "salt" (the impurities or A- and M″-based fluoride byproduct) dissolves in solution and is eliminated by centrifugation. Existing literature on 2D i-MXenes generally reports that washing with HCl and DI water effectively removes A- and M″-element fluoride byproducts, resulting in a pure 2D i-MXene structure.[43,44] Here, we employed a $(Mo_{2/3}Er_{1/3})_2AlC$ RE-based i-MAX phase for the synthesis of vacancy-ordered $Mo_{1.33}C$@Er using the conventional LiF/HCl etching method and carried out detailed structural characterization using X-ray diffraction (XRD), Raman spectroscopy, X-ray photoelectron spectroscopy (XPS), and scanning transmission electron Microscopy (STEM) of the resulting material. However, analyses present that prepared $Mo_{1.33}C$@Er is not in a pure form and show some impurity presence of Er-based fluoride byproducts, indicating that the standard synthesis and/or washing procedure may be insufficient. To assess the effect of byproducts on electrochemical behavior, comprehensive capacitance studies were conducted through cyclic voltammetry (CV), galvanostatic charge-discharge (GCD), and electrochemical impedance spectroscopy (EIS). Additionally, first-principles calculations have been performed on $Mo_{1.33}C$ 2D i-MXenes with various functional groups and their combinations, providing insights into the material's electronic nature.

2. EXPERIMENTAL PROCEDURE

2.1. Synthesis of the $(Mo_{2/3}Er_{1/3})_2AlC$ i-MAX Phase

To prepare the i-MAX phase $(Mo_{2/3}Er_{1/3})_2AlC$ polycrystalline samples, a nominal composition of all required materials was used in a conventional arc melting setup under an argon atmosphere with a water-cooled copper hearth. The materials used included Mo (Thermo Scientific, powder, 99.95%), C (Sigma-Aldrich, powder, 99.99%), Er (Ames Laboratory), and Al (Alfa Aesar, 99.999%). Initially, Mo and C powders were mixed in the appropriate atomic weight ratio (Mo:C = 1.333:1) using a pestle and mortar, and a homogeneous powder was formed, which was then mechanically pressed. Subsequently, Er and Al pieces were added to the pressed powder in an appropriate weight ratio ($Mo_{1.33}C$/Er/Al = 1:0.666:1) composition, and the mixture was arc-melted using an Edmund Buhler electric arc furnace.[31] The alloy was flipped and remelted 4−5 times to ensure a homogeneous ingot.

2.2. Synthesis of 2D $Mo_{1.33}C$@Er i-MXene

The conventional LiF/HCl method was used for synthesizing $Mo_{1.33}C$@Er. Initially, 20 mL of 9 M HCl was added to a small Nalgene bottle, which was immersed in an oil bath to maintain a constant temperature of 70 °C. Next, 0.6 g of the $(Mo_{2/3}Er_{1/3})_2AlC$ i-MAX phase and 0.4 g of LiF powder were gradually added to the solution. The mixture was stirred and allowed to etch for 7 days. After etching, the solution was transferred to a Falcon tube and washed once with HCl, and the supernatant was discarded. The sediment was then washed multiple times with DI water with a centrifugation speed of 4500 rpm for 20 min until the pH reached 6. Finally, the sediment was dried at 70 °C for 24 h to remove any residual solvent. A schematic presentation of the synthesis of 2D i-MXene is given in Figure 1a. To obtain delaminated nanosheets for characterization, 0.2 g of $Mo_{1.33}C$@Er powder was mixed with 5 mL of TBAOH and vortexed for 20 min. The mixture was then centrifuged at 4500 rpm for 1 h to remove excess TBAOH. The sediment was washed with DI water and centrifuged again under the same conditions until the pH reached neutral. Subsequently, 5 mL of DI water was added, and a final low-speed centrifugation at 3500 rpm for 1 h was performed. The resulting bluish supernatant contained the delaminated nanosheets, which were used for HRTEM analysis.

https://doi.org/10.1021/acsanm.5c04789
ACS Appl. Nano Mater. 2026, 9, 1089−1098

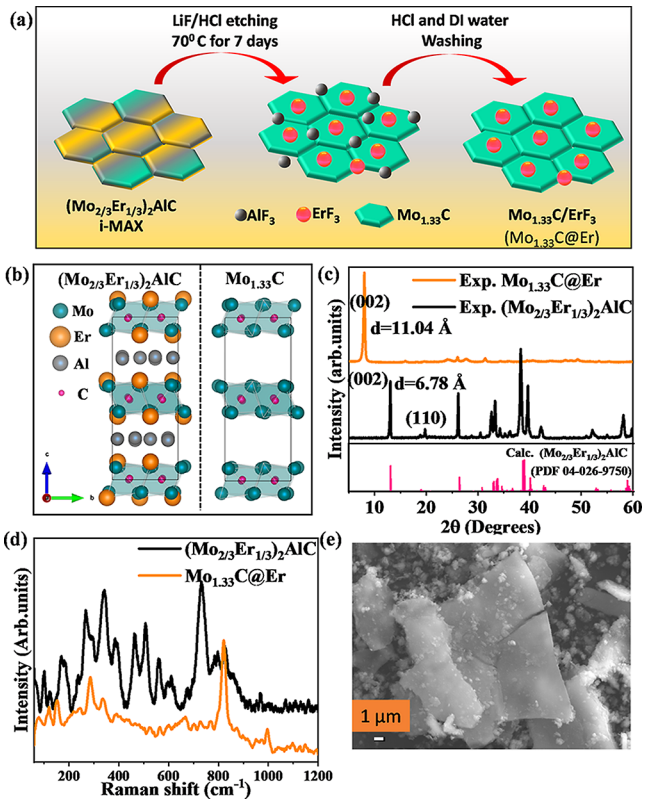

Figure 1. (a) Pictorial schematic depicting the synthesis of $Mo_{1.33}$@Er, (b) structural representation, (c) XRD pattern, (d) Raman spectra of the $(Mo_{2/3}Er_{1/3})_2AlC$ i-MAX phase and $Mo_{1.33}C$@Er, and (e) SEM image of prepared $Mo_{1.33}C$@Er.

3. MATERIALS CHARACTERIZATION

The structural and morphological characterization of $(Mo_{2/3}Er_{1/3})_2AlC$ and $Mo_{1.33}C$@Er was carried out by using various techniques. XRD analysis was performed using a Rigaku diffractometer with a Cu Kα source (40 kV, 15 mA) over a 2θ range from 5 to 60°. Raman measurements were conducted using a 785 nm laser. For morphological analysis, scanning electron microscopy (SEM) was utilized. Atomic structure analysis experiments were performed on an Analytical Scanning Transmission Electron Microscope (STEM) Thermo Fisher Talos F200X.

4. ELECTROCHEMICAL TESTING

Electrochemical measurements were carried out using a Biologic VMP3 workstation, with a Ag/AgCl electrode as the reference and a platinum electrode as the counter electrode. The working electrode slurry was prepared by mixing 5 mg of $Mo_{1.33}C$@Er, 1 mg of poly(vinylidene fluoride), and 100 μL of 1-methyl-2-pyrrolidinone. The mixture was sonicated for 1 h and subsequently brushed onto a microporous carbon cloth substrate (1.5 cm × 1.5 cm). The coated electrode was dried in an oven at 60 °C for 14 h.

5. COMPUTATIONAL METHOD

First-principles density functional theory (DFT) calculations were performed using the Vienna Ab initio Simulation Package (VASP).[51,52] Adapting initial structures from the experimentally observed $(Mo_{2/3}Er_{1/3})_2AlC$ i-MAX phase with $C2/c$ symmetry (space group number 15), crystal structures for 2D i-MXene and vacancy-containing $Mo_{1.33}C$ were created. In $Mo_{1.33}C$ i-MXene, Mo and vacancy (V) have in-plane chemical ordering in the metal layers, in which 2/3 of metal sites are Mo and 1/3 are V, such that the i-MXene sheet has a repeating three-site motif of (Mo−V−Mo). Vs occupy a distorted honeycomb sublattice in the a−c plane. Each V in $Mo_{1.33}C$ is surrounded by Mo atoms in all directions in such a way that V will not have another V as the nearest neighbor. The terminations (T_xs) protrude, sitting above and below the surface metal atoms, forming $Mo_{1.33}CT_x$. Then, the crystal structures of bare and functionalized $Mo_{1.33}C$ were optimized, updating ionic positions, minimizing the crystals' energy and forces, and treating electrons fully quantum mechanically. Projector augmented wave method-based pseudopotentials and Perdew−Burke−Ernzerhof functionals were used to address ion−electron interactions and exchange correlations, respectively.[53−55] Energy and force convergence criteria of 10^{-6} eV and 10^{-2} eV/Å, respectively, and a plane wave cutoff energy of 520 eV were employed to fully relax the atomic coordinates. The Monkhorst−Pack Γ-centered k-point meshes were chosen for Brillouin zone sampling in such a way that the k-point spacing is approximately 0.2/Å in each direction. Electronic iterations were carried out using the blocked Davidson algorithm[56] and reciprocal space projection operators. To avoid numerical problems due to the finite sampling of the Brillouin zone, Gaussian smearing with a width of 0.05 eV was employed. For each of the structures considered here, we have used a supercell of size 4 × 4 × 1.

6. RESULTS AND DISCUSSION

6.1. Characterization of $(Mo_{2/3}Er_{1/3})_2AlC$ i-MAX and $Mo_{1.33}C$@Er i-MXene

Figure 1b illustrates the crystal structures of the i-MAX phase $(Mo_{2/3}Er_{1/3})_2AlC$ and the corresponding i-MXene $Mo_{1.33}C$, modeled by using VESTA software. The i-MAX phase exhibits a monoclinic structure with in-plane ordering of M′ and M″ atoms, which generates a (110) plane and shows a peak near 20° in the recorded XRD pattern, which is a fingerprint of the i-MAX phase, which is absent in traditional MAX phases.[22] Here, the in-plane ordering peak for $(Mo_{2/3}Er_{1/3})_2AlC$ i-MAX phase is at 19.89°, which matches well with the PCD database (1959003, PDF 04026-9750), confirming the formation of the i-MAX phase structure.[44] The (002) diffraction peak shifts from 13.03° to 7.99°, indicating an expansion of the c-lattice parameter from 6.78 Å in the i-MAX phase to 11.04 Å in the multilayered solid-solution i-MXene after etching. The intensity of the (002) peak in $Mo_{1.33}C$@Er is significantly higher compared with its i-MAX phase, suggesting a highly crystalline phase. Additionally, the XRD pattern of the etched material reveals new peaks at 24.6° and 27.8° and other minor peaks at higher degrees, absent in the pristine $(Mo_{2/3}Er_{1/3})_2AlC$ phase. Matching these peaks with the ICDD database indicates the formation of ErF_3,[57] which is attributed to the reaction between Er and fluorine during etching, as also shown in Figure 1a. Another significant observation is the disappearance of the peak near 19.89° in the XRD pattern of $Mo_{1.33}C$@Er, suggesting that the ordered arrangement of Mo and Er atoms in the i-MAX phase is disrupted following the removal of Er during etching. Once the ErF_3 byproduct forms, unlike AlF_3, it becomes insoluble in HCl and DI water, remaining in the prepared $Mo_{1.33}C$@Er. Removing ErF_3 is possible only using perchloric acid, a strong acid that may oxidize the resulting $Mo_{1.33}C$@Er. This observation is further supported by XPS analysis and STEM measurements. The SEM micrograph (Figure S1) of i-MAX

https://doi.org/10.1021/acsanm.5c04789
ACS Appl. Nano Mater. 2026, 9, 1089−1098

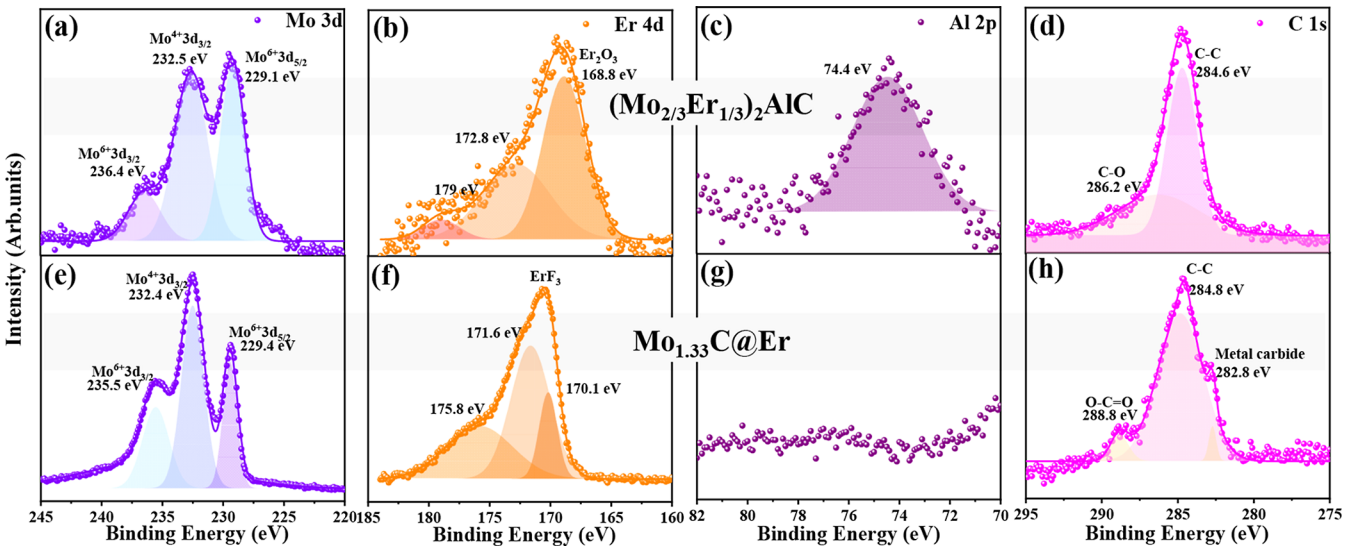

Figure 2. (a, e) Mo 3d, (b, f) Er 4d, (c, g) Al 2p, and (d, h) C 1s spectra of $(Mo_{2/3}Er_{1/3})_2AlC$ and $Mo_{1.33}C$@Er, respectively.

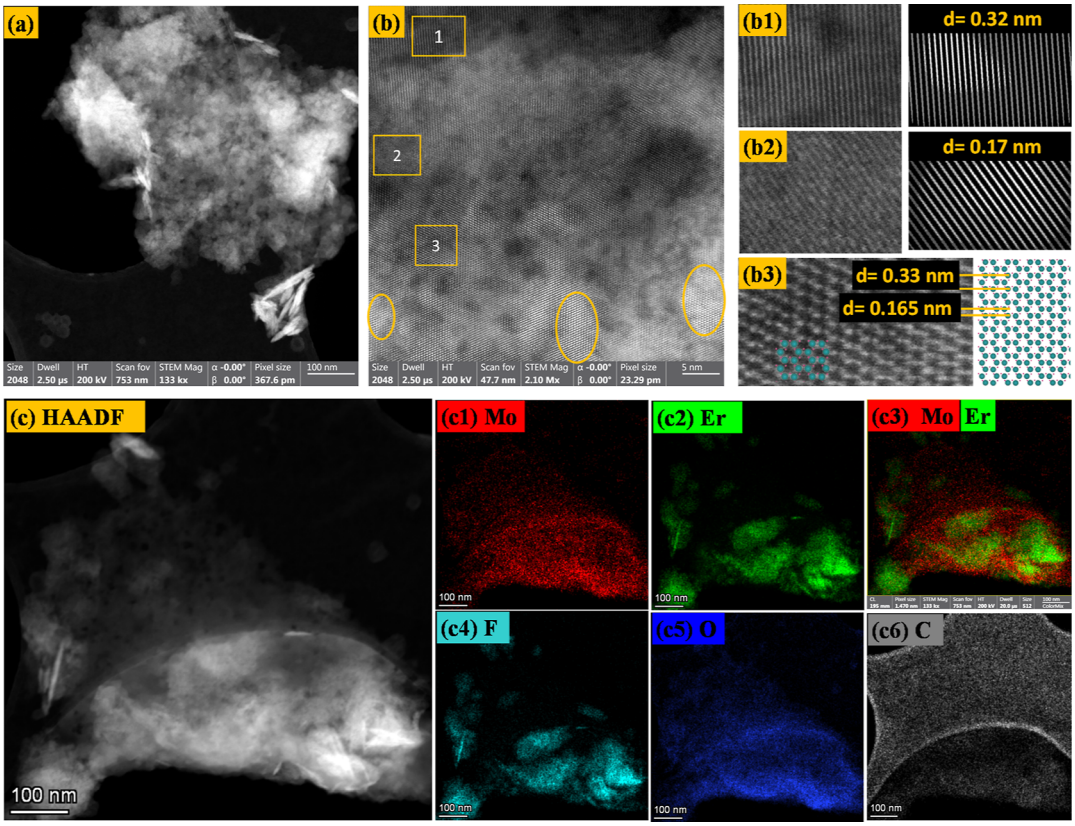

Figure 3. STEM HAADF micrograph images of $Mo_{1.33}C$@Er at (a) 100 nm and (b) 5 nm resolution, (b1−b3) enlarged view of small areas 1, 2, and 3 marked in image (b). (c) STEM HAADF image at 100 nm with its EDS mapping (c1) Mo, (c2) Er, (c3) Mo, Er, (c4) F, (c5) O, and (c6) C of the prepared sample.

shows the irregular shape of the particles with sharp edges and varying thickness. Figure 1c shows the Raman spectra for $(Mo_{2/3}Er_{1/3})_2AlC$ and its corresponding $Mo_{1.33}C$@Er. The Raman shift wavenumbers are provided in Table S1. According to the study by Champagne et al.,[36,58] theoretical phonon calculations show that Raman modes below ∼170 cm^{-1} arise from vibrations involving RE, Mo, and Al, ∼170−260 cm^{-1} modes are primarily associated with Mo and Al, and bands above ∼500 cm^{-1} correspond to C atom vibrations. We observed that closely spaced peaks were present in the $(Mo_{2/3}Er_{1/3})_2AlC$ phase but absent in the Raman spectra of $Mo_{1.33}C$@Er. Table S1 lists the possible vibrational modes for both samples, including contributions from erbium oxide and molybdenum oxide impurities present in the i-MAX phase,[44] as well as residual ErF_3 detected in $Mo_{1.33}C$@Er, which also contributes to the observed Raman signals. The morphology of $Mo_{1.33}C$@Er, as depicted in Figures 1e and S2a−d, transitions into a sheet-like morphology, a characteristic structure of 2D

https://doi.org/10.1021/acsanm.5c04789
ACS Appl. Nano Mater. 2026, 9, 1089−1098

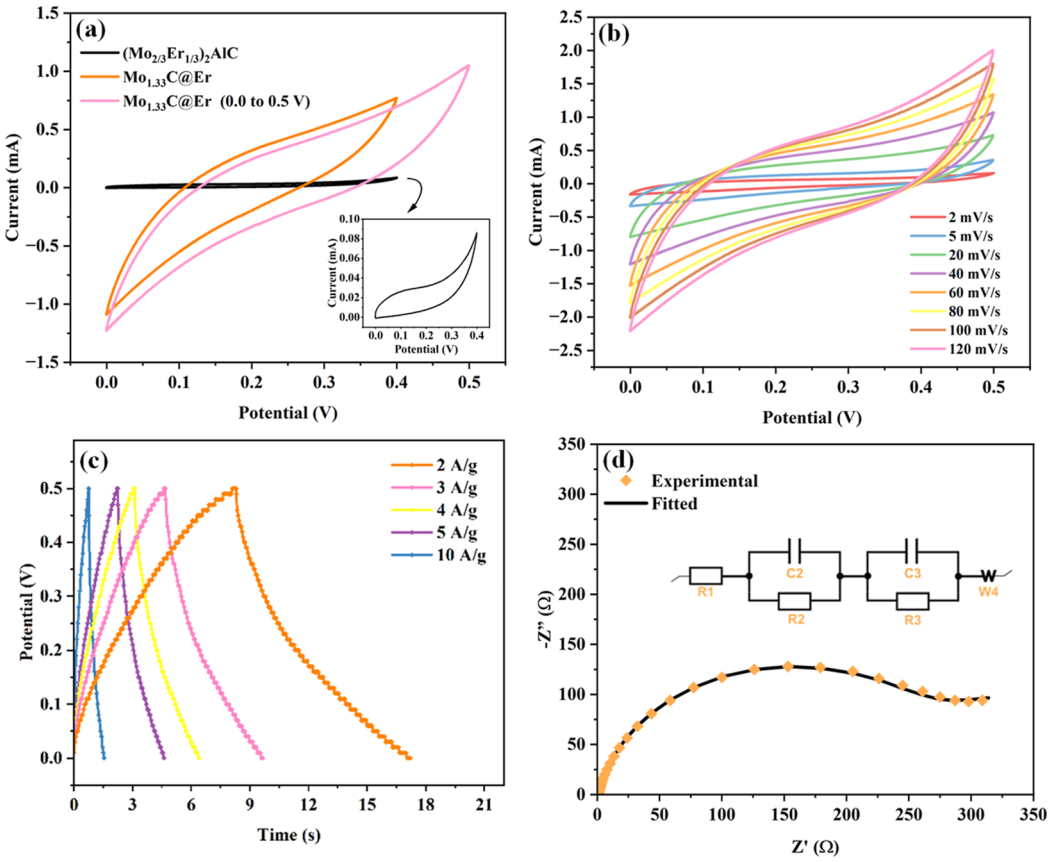

Figure 4. (a) Comparative cyclic voltammetry (CV) curves of the $(Mo_{2/3}Er_{1/3})_2AlC$ i-MAX phase and $Mo_{1.33}C$@Er at a scan rate of 100 mV/s, (b) CV curves of $Mo_{1.33}C$@Er at increasing scan rates, (c) galvanostatic charge and discharge (GCD) curves of $Mo_{1.33}C$@Er at increasing current density, and (d) Nyquist plot of the electrochemical impedance of $Mo_{1.33}C$@Er, fitted with an equivalent circuit.

MXenes. Along with the sheets, small particulates are also observed, which likely correspond to residual ErF_3 byproducts formed during etching.

XPS measurements were performed for $(Mo_{2/3}Er_{1/3})_2AlC$ (Figures 2a–d and S3a–d) and $Mo_{1.33}C$@Er (Figures 2e–h and S3e–h). Peak fitting and deconvolution were carried out for all elements, and the results were analyzed. The Mo 3d spectra (Figure 2a,e) exhibit Mo $3d_{5/2}$ and Mo $3d_{3/2}$ peaks for both samples. The Er 4d spectra (Figure 2b,f) display an Er_2O_3 peak in the i-MAX phase, indicating oxide-based impurities in pristine i-MAX. The presence of Er_2O_3 slightly affects the LiF/HCl etching process by consuming H^+ and F^- and forming ErF_3, which ultimately results in an impure $Mo_{1.33}C$@Er. Additionally, the Er 4d spectra in $Mo_{1.33}C$@Er show a shift to higher binding energy and the presence of an ErF_3 (171.6 eV) peak, consistent with XRD results, suggesting that Er reacts with fluorine during the etching process and forms ErF_3. The lower-energy peak at 170.1 eV is related to Er–O bonding, while the higher-energy peak corresponds to Er $4d_{3/2}$.[59] The Al 2p peak (Figure 2c,g) is present in $(Mo_{2/3}Er_{1/3})_2AlC$ but absent in $Mo_{1.33}C$@Er, confirming the successful removal of Al. The C 1s spectra (Figure 2d,h) for the i-MAX phase show C–C and C–O peaks, and the 2D i-MXene displays a metal carbide, C–C, and carboxyl peak, further confirming 2D i-MXene formation. Figure S3a,e presents survey spectra, highlighting all the elements present in both samples. Specifically, the O 1s spectra (Figure S3b,f) for $(Mo_{2/3}Er_{1/3})_2AlC$ indicate the presence of metal carbonates and oxides, while the O 1s spectra for $Mo_{1.33}C$@Er show MoO_2 and metal hydroxide peaks. Additionally, the $Mo_{1.33}C$@Er spectra display the ErF_3 peak in the F 1s spectra (Figure S3g) along with a Cl 2p peak (Figure S3h), both of which are absent in the $(Mo_{2/3}Er_{1/3})_2AlC$ phase (Figure S3c,d), as chlorine and fluorine originate from the etchant. Accordingly, the termination stoichiometry of $Mo_{1.33}C$@Er can be expressed as $Mo_{1.33}C\ O_{0.46}(OH)_{0.44}F_{1.14}$. These results confirm that the as-etched $Mo_{1.33}C$@Er surface is predominantly fluorine-terminated with comparable but smaller contributions from –O and –OH terminations.

To investigate the structure of prepared $Mo_{1.33}C$@Er, HRSTEM measurements were conducted using high-resolution Z contrast imaging with a high-angle dark field (HAADF) detector, as shown in Figure 3. For the analysis, a colloidal solution of $Mo_{1.33}C$@Er was prepared using the TBAOH intercalation technique, resulting in a bluish solution (Figure S4). Figure S5 presents the HAADF image and elemental mapping of the $(Mo_{2/3}Er_{1/3})_2AlC$ i-MAX phase (before etching). In the parent i-MAX structure, Mo and Er exhibit a similar distribution pattern. However, after etching, the elemental mapping of Mo and Er reveals a distinct change in their distribution. Figure 3a displays a lower magnification STEM image of $Mo_{1.33}C$@Er. Higher magnification STEM images are shown in Figure 3b, b1,b2,b3 are enlarged views of the area of interest. As we observed in Figure 3b, the brightest spots in the image correspond to Er atoms, as Er is heavier than Mo and carbon; these bright dots are prominent in certain regions, highlighted with circles, while in other areas, they are less distinct, which suggest Er atoms are not uniformly

https://doi.org/10.1021/acsanm.5c04789
ACS Appl. Nano Mater. 2026, 9, 1089–1098

distributed and instead form ErF_3, which just remained in $Mo_{1.33}C$@Er. Figure 3b1−b3, showing interplanar spacings of 0.32 and 0.17 nm, corresponding to the interplanar spacing of Mo atoms, as depicted in Figure 3b3, which reveals the hexagonal structural arrangement of Mo atoms when viewed along the [001] direction. In these images, C atoms exhibit negligible contrast, making only the Mo atoms visible. In our STEM images, the lattice contrast appears less defined, primarily due to the coexistence of $Mo_{1.33}C$ layers with residual ErF_3, which diminishes the visibility of vacancy ordering. To understand vacancy formation in $Mo_{1.33}C$@Er, we compared the simulated [001] projections of the $(Mo_{2/3}Er_{1/3})_2AlC$ phase (Figure S6a) and the corresponding $Mo_{1.33}C$ model (Figure S6b), generated using VESTA, with the experimental HRSTEM image of the prepared sample (Figure 3b3). In the $(Mo_{2/3}Er_{1/3})_2AlC$ structure, Er atoms occupy the centers of the Mo hexagons (see Figure S6a). During etching, these Er atoms are removed, creating characteristic vacancies at the hexagon centers in the i-MXene model (Figure S6b). When we compare this model with the experimental HRSTEM image of $Mo_{1.33}C$@Er (Figure 3b3), we observe the expected hexagonal arrangement of Mo atoms with empty centers, indicating the removal of Er and the formation of vacancies. STEM HAADF EDS mapping reveals that bright regions (in Figure 3c) correspond to Er and F, as shown in the mapping data (Figure 3c2,c4), while the lighter areas correspond to Mo (Figure 3c1), as seen from the Mo mapping data. The Er and F mappings appear identical, whereas Figure 3c3 shows that Mo and Er atoms are unevenly distributed. This suggests that Er atoms were etched out from the in-plane-ordered $(Mo_{2/3}Er_{1/3})_2AlC$ structure but persisted in the final sample as ErF_3, since this byproduct is insoluble in the washing solvent. As a result, the product is a mixture of $Mo_{1.33}C$ and ErF_3. Additionally, O and C mapping signals were detected (Figure 3c5,c6), originating from surface functional groups and the overall carbon framework of $Mo_{1.33}C$@Er.

6.2. Electrochemical Performance of $Mo_{1.33}C$@Er 2D i-MXene

To get insight into the electrochemical behavior of prepared $Mo_{1.33}C$@Er, CV, GCD, and EIS were performed in a three-electrode system using 1 M H_2SO_4 electrolyte. In Figure 4a, $Mo_{1.33}C$@Er exhibited a significant increase in current density compared to its precursor, $(Mo_{2/3}Er_{1/3})_2AlC$. Both $Mo_{1.33}C$@Er and $(Mo_{2/3}Er_{1/3})_2AlC$ electrodes were swept over a potential range of 0.0−0.4 V, where the current response and enclosed CV curve area directly correlate with their energy storage capability. The enhanced current response in $Mo_{1.33}C$@Er suggests that the removal of aluminum during the etching process resulted in a more open and conductive surface. Using the formula $C = \frac{\int_{V_1}^{V_2} I\,dv}{2sm\Delta V}$, where C is the specific capacitance, $\int_{V_1}^{V_2} I\,dv$ is the integral CV curve area, s is the scan rate, m is the mass of the active material, and ΔV is the potential window,[60,61] the $(Mo_{2/3}Er_{1/3})_2AlC$ i-MAX phase showed a specific capacitance of 78.8 mF/g, while $Mo_{1.33}C$@Er exhibited a significantly higher value of 1904 mF/g, marking a 24-fold improvement. When the potential window was extended to 0.5 V, the specific capacitance of $Mo_{1.33}C$@Er further increased to 2214.8 mF/g. The same could not be performed with $(Mo_{2/3}Er_{1/3})_2AlC$ because when scanned over a wider potential window, it showed instability in CV behavior (Figure S7). Starting from 0.0 to 0.5 V, the charging and discharging curves displayed an unusual overlap or crossing, indicating poor electron kinetics and low conductivity. However, $Mo_{1.33}C$@Er maintained stable CV profiles up to 0.0−0.7 V, demonstrating better charge storage performance across an extended applied potential range (Figure S8). The significant increase in capacitance upon converting i-MAX to i-MXene could be explained by the emergence of termination-derived surface electronic states, as observed in the DFT analysis, which then promotes rapid faradaic charge storage. $Mo_{1.33}C$@Er exhibits Mo 4d/O 2p hybridization at the Fermi level, creating high-density surface electronic states that act as fast redox-active sites. In Figure 4b, the CV curves of $Mo_{1.33}C$@Er were recorded at increasing scan rates of within 2 mV/s to 120 mV/s. The typical increase in the CV area and decline in specific capacitance with increasing scan rate were observed. The calculated values were 22.1, 20.2, 11.7, 8.4, 6.8, 5.7, 4.9, and 4.4 F/g at scan rates of 2, 5, 20, 40, 60, 80, 100, and 120 mV/s, respectively. The GCD profiles of $Mo_{1.33}C$@Er (Figure 4c) exhibit stable charge−discharge behavior with good Coulombic efficiency, delivering specific capacitances of 35.6, 29.9, 13.8, 23.6, and 15.8 F g^{-1} at current densities of 2, 3, 4, 5, and 10 A g^{-1}, respectively. Under continuous cycling, the material preserves 86.7% of its initial capacitance after 1000 cycles, which gradually declines to 62.4% after 5000 cycles (Figure S9). Considering the heterogeneous surface chemistry of $Mo_{1.33}C$@Er as shown in the Raman spectroscopy, XPS, and DFT results, the presence of irreversible surface redox processes could be likely, which manifested in the early cycling stages. As these reactions become exhausted or inactive over time, the available active sites decrease, resulting in the progressive loss of capacitance. The relationship between the scan rate and specific capacitance was studied to determine the charge storage mechanisms in $Mo_{1.33}C$@Er. The Trasatti method was used to distinguish between electric double layer capacitance (EDLC) and pseudocapacitance (PS). This technique takes advantage of the different dependencies of EDLC and PS on the scan rate due to their distinct charge storage mechanisms.[62,63] At higher scan rates (s), electrolyte ions are restricted to interacting only with the outer surface of the electrode material, making capacitance (C) primarily dependent on surface interactions between the outer electrode and the electrolyte.[62] Consequently, the y-intercept of the $s^{-1/2}$ vs C plot represents the capacitance contribution from surface-controlled EDLC (Figure S10a). This dominance could again be traced to the surface-localized electronic states of the Mo 4d/O 2p hybridization at the Fermi level, as mentioned in the electronic properties. Conversely, at lower scan rates, diffusion effects take precedence, allowing electrolyte ions to reach both the inner and outer electrode surfaces.[62] In this scenario, the y-intercept of the linear fit from $s^{1/2}$ vs $1/C$ corresponds to the total capacitance (Figure S10b). The difference between the total capacitance and the contribution from EDLC accounts for the pseudocapacitive contribution. Based on these calculations, pseudocapacitance dominates the storage mechanism, constituting 98.05% of the total capacitance, while the remaining 1.95% is attributed to EDLC (Figure S10c). To further understand the charge storage mechanism and kinetics of $Mo_{1.33}C$@Er, EIS was conducted, and the corresponding Nyquist plot is shown in Figure 4d. The fitted equivalent circuit, $R_1 + (C_2/R_2) + (C_3/R_3) + W_4$, using the Zfit and PseudoC functions of Biologic EC-Lab software provided valuable information on the charge transfer, pseudocapacitive

https://doi.org/10.1021/acsanm.5c04789
ACS Appl. Nano Mater. 2026, 9, 1089−1098

Table 1. Equivalent Circuit Fitting Parameters from the EIS Measurement of $Mo_{1.33}C$@Er

R_1 (Ω)	C_2 (F)	R_2 (Ω)	C_3 (F)	R_3 (Ω)	W_4 ($\Omega\ s^{-1/2}$)
0.8965	1.914×10^{-3}	152.1	50.9×10^{-6}	288.1	0.3343×10^{-12}

behavior, and ion diffusion limitations of $Mo_{1.33}C$@Er.[64,65] The fitted parameters are summarized in Table 1. The low R_1 value (0.8965 Ω), which is the solution resistance, suggests minimal resistance from the ionic environment. The spectrum exhibits a large semicircle in the high-to-medium frequency range, indicative of high charge-transfer resistance (R_2 = 152.1 Ω, R_3 = 288.1 Ω). This suggests that while redox reactions occur, electron transport within the material is hindered, likely due to the presence of ErF_3 that could act as an insulating layer.[66] Combining the insight gained from EIS and Trasatti analysis, it could be suggested that $Mo_{1.33}C$@Er displays distinctly surface-dominated pseudocapacitive behavior.

6.3. Electronic Properties of $Mo_{1.33}C$ 2D i-MXene

Recognizing the impact of surface terminations on MXene electronic properties, we investigated $Mo_{1.33}C$ through DFT calculations, considering both pristine and functionalized forms. The optimized structures remain monoclinic with C_2/c crystal symmetry. The eV/atom normalized formation energy is the largest negative (−0.3491) for oxygen−fluorine mix-terminated $Mo_{1.33}C(OF)x$ among the bare, −O, −F, and −O/−F mix-terminated i-MXenes considered in this study, indicating that oxygen−fluorine mix-terminated i-MXene is energetically favorable. To measure how strongly the functional groups are bonded with the parent i-MXene, the binding energy E_B per functional group (T_x) is calculated using the following equation:

$$E_{B/T_x} = \frac{1}{n}[E(Mo_{1.33}CT_x) - E(Mo_{1.33}C) - nE(T_x)]$$

where $E()$ denotes the energy of respective systems in their stable states. With $E_{B/T_x} = -1.071$ eV/T_x, −O/−F mix-terminated i-MXene has the largest negative value for E_{B/T_x}. The E_{B/T_x} follows the $E_{B/OF} < E_{B/F} < E_{B/O}$ inequality, indicating that fluorine bonds more strongly than oxygen, and the bonding is even stronger in the mix-terminated one. Figure 5a−d represents band structures, and Figure 5e−h shows orbital projected density of states for bare, O-terminated, F-terminated, and −O and −F mix-terminated $Mo_{1.33}C$. The energy level is shifted by the Fermi level (E_F). The chosen k-point mesh follows the path of Γ (0,0,0) → Z (0,−1/2,1/2) → M (−1/2,−1/2,1/2) → A (−1/2,0,0) → Γ (0,0,0) → V (0,0,1/2). Band structures show that bare and all functionalized $Mo_{1.33}C$ are metallic. Nonzero density of states at the Fermi level confirms the metallic nature. At the Fermi level and conduction band, the density states are dominated by Mo 4d states for each of the structures. At the valence band, we witness the hybridization of Mo 4d states with C 2p states, O 2p states, and/or F 2p states. O 2p's hybridization is stronger in O-terminated $Mo_{1.33}C$ than F 2p's hybridization in F-terminated $Mo_{1.33}C$. In O-terminated $Mo_{1.33}C$, O 2p has a significant contribution at the Fermi level, while that contribution shifts to a higher energy value, making it significant in the conduction band. The metallic nature is also preserved in the −O/−F mix-terminated $Mo_{1.33}C$. The mix-termination caused enhanced O 2p contribution in the conduction band compared to the other single-atom-type surface termination.

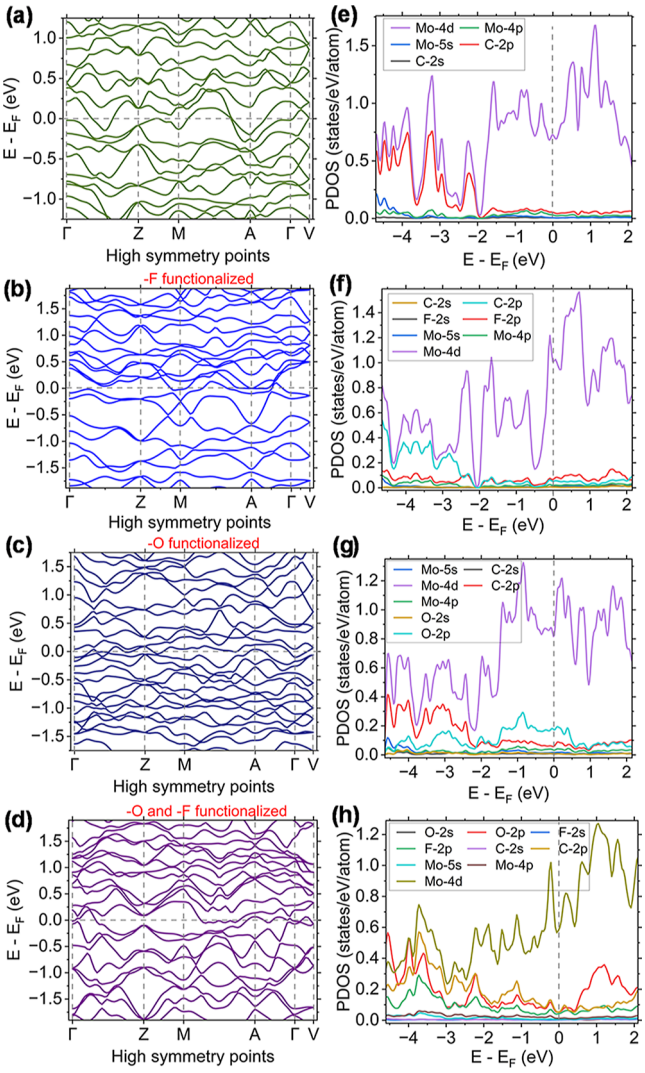

Figure 5. (a−d) Band structures and (e−h) orbital projected density of states for bare $Mo_{1.33}C$, oxygen-functionalized $Mo_{1.33}C$, fluorine-functionalized $Mo_{1.33}C$, and mix-terminated $Mo_{1.33}C$ functionalized with oxygen and fluorine.

7. CONCLUSIONS

Using the LiF/HCl mild etching method, 2D i-MXene can be prepared; however, achieving a pure i-MXene from the $(Mo_{2/3}Er_{1/3})_2AlC$ i-MAX phase presents significant challenges. This is primarily due to the formation of RE fluoride compounds (e.g., ErF_3) in the fluorine-rich etching environment, driven by the strong electronegativity difference between the Er and F atoms. These fluoride byproducts are largely insoluble in HCl and deionized water, making them difficult to remove through conventional washing procedures. Results conclude that ErF_3 remains embedded in $Mo_{1.33}C$@Er due to the insolubility of this compound in common acids, emphasizing the need to refine washing procedures or synthesis routes for 2D i-MXenes derived from RE-based i-MAX phases. To achieve high-purity 2D i-MXenes, it is essential to evaluate the solubility of the resulting byproducts and, going forward, to

https://doi.org/10.1021/acsanm.5c04789
ACS Appl. Nano Mater. 2026, 9, 1089−1098

assess the viability of different i-MAX precursors through comprehensive structural characterization. Additionally, $Mo_{1.33}C$@Er exhibits a specific capacitance of 2.21 F/g at a scan rate of 2 mV/s and a potential window of 0−0.5 V. However, EIS measurements reveal a relatively high charge-transfer resistance, suggesting that electron transport is hindered by the presence of residual ErF_3 byproducts, likely to form an insulating layer, thereby fading the overall electrochemical performance. Prior reports on $Mo_{1.33}C$ 2D i-MXene prepared from the $(Mo_{2/3}Sc_{1/3})_2AlC$ i-MAX phase demonstrate that ordered vacancies can enable high capacitance and efficient ion transport.[21] Therefore, we have framed the material as a promising candidate for electrochemical energy storage applications once the synthesis procedure is further improved. DFT calculations show both the bare and functionalized $Mo_{1.33}C$ are metallic. 4d states of Mo, 2p states of C, and 2p states of O and/or F have a significant contribution to the total density of states of $Mo_{1.33}CT_x$.

■ ASSOCIATED CONTENT

Supporting Information

The Supporting Information is available free of charge at https://pubs.acs.org/doi/10.1021/acsanm.5c04789.

Raman lines for $(Mo_{2/3}Er_{1/3})_2AlC$ i-MAX and $Mo_{1.33}C$@Er i-MXene; electrochemical performance; SEM images; the XPS survey; O 1s, F 1s, and Cl 2p spectra; bluish-colored colloidal dispersion of delaminated $Mo_{1.33}C$@Er i-MXene; STEM-HAADF image; EDS elemental maps; VESTA-generated structural models; cyclic voltammetry curves; cycling stability performance; GCD curves for the first and 5000th cycles; and EDLC and pseudocapacitive contributions of $Mo_{1.33}C$@Er i-MXene (PDF)

■ AUTHOR INFORMATION

Corresponding Author

Bhoj Raj Gautam − *Department of Chemistry, Physics, and Materials Science, Fayetteville State University, Fayetteville, North Carolina 28301, United States;* orcid.org/0000-0001-5083-6250; Email: bgautam@uncfsu.edu

Authors

Nisha Hiralal Makani − *Department of Chemistry, Physics, and Materials Science, Fayetteville State University, Fayetteville, North Carolina 28301, United States*

Chandra M. Adhikari − *Department of Chemistry, Physics, and Materials Science, Fayetteville State University, Fayetteville, North Carolina 28301, United States;* orcid.org/0000-0002-7776-0441

Shanna Marie M. Alonzo − *Department of Chemistry, North Carolina A&T State University, Greensboro, North Carolina 27411, United States*

Bishnu Prasad Bastakoti − *Department of Chemistry, North Carolina A&T State University, Greensboro, North Carolina 27411, United States;* orcid.org/0000-0002-4651-7393

Binod K. Rai − *Savannah River National Laboratory, Aiken, South Carolina 29808, United States*

Complete contact information is available at: https://pubs.acs.org/10.1021/acsanm.5c04789

Notes

The authors declare no competing financial interest.

■ ACKNOWLEDGMENTS

This work was supported by DOE BES award number DE-SC0024611. SRNL work was produced by Battelle Savannah River Alliance, LLC under Contract No. 89303321CEM000080 with the U.S. Department of Energy. Publisher acknowledges the U.S. Government license to provide public access under the DOE Public Access Plan (https://www.energy.gov/downloads/doepublic-access-plan).

■ REFERENCES

(1) Gomollón-Bel, F. Ten Chemical Innovations That Will Change Our World: IUPAC Identifies Emerging Technologies in Chemistry with Potential to Make Our Planet More Sustainable. *Chem. Int.* **2019**, *41* (2), 12−17.

(2) Zhang, D.; Shah, D.; Boltasseva, A.; Gogotsi, Y. MXenes for Photonics. *ACS Photonics* **2022**, *9* (4), 1108−1116.

(3) Gogotsi, Y. The Future of MXenes. *Chem. Mater.* **2023**, *35* (21), 8767−8770.

(4) Ahmed, B.; Ghazaly, A. E.; Rosen, J.; Ahmed, B.; El Ghazaly, A.; Rosen, J. I-MXenes for Energy Storage and Catalysis. *Adv. Funct. Mater.* **2020**, *30* (47), 2000894.

(5) Anasori, B.; Lukatskaya, M. R.; Gogotsi, Y. 2D Metal Carbides and Nitrides (MXenes) for Energy Storage. *Nat. Rev. Mater.* **2017**, *2* (2), 16098.

(6) Zhang, C.; Ma, Y.; Zhang, X.; Abdolhosseinzadeh, S.; Sheng, H.; Lan, W.; Pakdel, A.; Heier, J.; Nüesch, F. Two-Dimensional Transition Metal Carbides and Nitrides (MXenes): Synthesis, Properties, and Electrochemical Energy Storage Applications. *Energy Environ. Mater.* **2020**, *3* (1), 29−55.

(7) Akhter, R.; Maktedar, S. S. MXenes: A Comprehensive Review of Synthesis, Properties, and Progress in Supercapacitor Applications. *J. Materiomics* **2023**, *9* (6), 1196−1241.

(8) Anasori, B.; Lukatskaya, M. R.; Gogotsi, Y. 2D Metal Carbides and Nitrides (MXenes) for Energy Storage. In *MXenes*; Jenny Stanford Publishing, 2023; pp 677−722.

(9) Chan, K. C.; Guan, X.; Zhang, T.; Lin, K.; Huang, Y.; Lei, L.; Georgantas, Y.; Gogotsi, Y.; Bissett, M. A.; Kinloch, I. A. The Fabrication of Ti_3C_2 and Ti_3CN MXenes by Electrochemical Etching. *J. Mater. Chem. A* **2024**, *12* (37), 25165−25175.

(10) Ajmal, Z.; Qadeer, A.; Singh, K.; Al Mahmud, A.; Lakhan, M. N.; Pradeep, H.; Hussain, B.; Ullah, A.; Khan, H. R.; Ibrahim, E. H.; Kewate, O. J.; Cui, J.; Rosaiah, P.; Akkinepally, B.; Hussain, I.; Shuhang, W. A Comprehensive Review on MXenes for Various Applications. *Appl. Energy* **2025**, *397*, 126136.

(11) Alam, M. S.; Chowdhury, M. A.; Kowser, M. A.; Islam, M. S.; Islam, M. M.; Khandaker, T. Advances of MAX Phases: Synthesis, Characterizations and Challenges. *Eng. Rep.* **2024**, *6* (8), No. e12911.

(12) Murali, G.; Reddy Modigunta, J. K.; Park, Y. H.; Lee, J. H.; Rawal, J.; Lee, S. Y.; In, I.; Park, S. J. A Review on MXene Synthesis, Stability, and Photocatalytic Applications. *ACS Nano* **2022**, *16* (9), 13370−13429.

(13) Naguib, M.; Kurtoglu, M.; Presser, V.; Lu, J.; Niu, J.; Heon, M.; Hultman, L.; Gogotsi, Y.; Barsoum, M. W. Two-Dimensional Nanocrystals Produced by Exfoliation of Ti_3AlC_2. *Adv. Mater.* **2011**, *23* (37), 4248−4253.

(14) Guan, G.; Guo, F. A Review of Nb_2CTx MXene: Synthesis, Properties and Applications. *Batteries* **2023**, *9* (4), 235.

(15) Etzkorn, J.; Ade, M.; Hillebrecht, H. V_2AlC, V_4AlC_{3-x} ($x \approx 0.31$), and $V_{12}Al_3C_8$: Synthesis, Crystal Growth, Structure, and Superstructure. *Inorg. Chem.* **2007**, *46* (18), 7646−7653.

(16) Sijuade, A. A.; Bellevu, F. L.; Devendhar Singh, S. K.; Rahman, M. M.; Arnett, N.; Okoli, O. I. Processing of V_2AlC MAX Phase: Optimization of Sintering Temperature and Composition. *Ceram. Int.* **2024**, *50* (2), 3733−3738.

(17) Mendoza-Sánchez, B.; Samperio-Niembro, E.; Dolotko, O.; Bergfeldt, T.; Kübel, C.; Knapp, M.; Shuck, C. E. Systematic Study of the Multiple Variables Involved in V_2AlC Acid-Based Etching Processes, a Key Step in MXene Synthesis. *ACS Appl. Mater. Interfaces* **2023**, *15* (23), 28332−28348.
(18) Zhang, W.; Li, S.; Fan, S.; Zhang, X.; Fan, X.; Bei, G. $Ti_3AlC_{2-y}N_y$ Carbonitride MAX Phase Solid Solutions with Tunable Mechanical, Thermal, and Electrical Properties. *J. Adv. Ceram.* **2024**, *13* (9), 1473−1481.
(19) Anasori, B.; Xie, Y.; Beidaghi, M.; Lu, J.; Hosler, B. C.; Hultman, L.; Kent, P. R. C.; Gogotsi, Y.; Barsoum, M. W. Two-Dimensional, Ordered, Double Transition Metals Carbides (MXenes). *ACS Nano* **2015**, *9* (10), 9507−9516.
(20) Feng, X.; Bai, T.; Xiao, B. Prediction of Surface Termination Preference of Out-of-Plane Ordered Double-Transition Metal MXenes (o-MXenes) from First-Principles Calculations. *J. Phys. Conf. Ser.* **2022**, *2321* (1), 012012.
(21) Tao, Q.; Dahlqvist, M.; Lu, J.; Kota, S.; Meshkian, R.; Halim, J.; Palisaitis, J.; Hultman, L.; Barsoum, M. W.; Persson, P. O. Å.; Rosen, J. Two-Dimensional $Mo_{1.33}C$ MXene with Divacancy Ordering Prepared from Parent 3D Laminate with in-Plane Chemical Ordering. *Nat. Commun.* **2017**, *8* (1), 14949.
(22) Dahlqvist, M.; Lu, J.; Meshkian, R.; Tao, Q.; Hultman, L.; Rosen, J. Prediction and Synthesis of a Family of Atomic Laminate Phases with Kagomé-like and in-Plane Chemical Ordering. *Sci. Adv.* **2017**, *3* (7), No. e1700642.
(23) Dahlqvist, M.; Petruhins, A.; Lu, J.; Hultman, L.; Rosen, J. Origin of Chemically Ordered Atomic Laminates (i-MAX): Expanding the Elemental Space by a Theoretical/Experimental Approach. *ACS Nano* **2018**, *12* (8), 7761−7770.
(24) Sun, S.; Ma, Z.; Chen, Z.; Liu, P.; Song, Y.; Lu, Q.; Fu, X.; Wang, Q.; Cui, W. The Crystallographic Structure and Properties of Novel Quaternary Nanolaminated Rare-Earth-Cr-Based i-MAX Phases. *Acta Mater.* **2023**, *242*, 118479.
(25) Chong, H.; Wang, C.; Guo, H.; Sun, S.; Gong, W.; Fu, X.; Huang, X.; Ma, S.; Liu, G.; Wang, Q.; Cui, W. Investigations on the Crystallographic Stacking Disordering and Properties of Novel Ga-Containing in-Plane Chemically Ordered $(Cr_{2/3}R_{1/3})_2GaC$ (R = Y, Tb - Lu) i-MAX Phases. *Acta Mater.* **2024**, *277*, 120213.
(26) Tsyganov, A.; Vikulova, M.; Zotov, I.; Morozova, N.; Korotaev, E.; Grapenko, O.; Gorokhovsky, A.; Gorshkov, N. Synthesis of 2D $Mo_{1.33}CT_z$ i-MXene with Ordered Vacancies by Hydrothermal Etching of $(Mo_{2/3}Y_{1/3})_2AlC$ i-MAX Phase. *Inorg. Chem. Commun.* **2024**, *170*, 113493.
(27) Cheng, J.; Zhang, Q.; Fu, S.; Wan, D.; Bao, Y.; Chu, L.; Feng, Q.; Hu, C. Synthesis, Microstructure and Properties of Ternary Layered i-MAX $(Mo_{2/3}M_{1/3})_2AlC$ (M = Sc and Lu) Ceramics Fabricated by Spark Plasma Sintering. *J. Eur. Ceram. Soc.* **2023**, *43* (15), 6774−6782.
(28) ElMelegy, T. A.; Sokol, M.; Barsoum, M. W. Enhanced Yield Synthesis of Bulk Dense $(M_{2/3}Y_{1/3})_2AlC$ (M = Cr, W, Mo) in-Plane Chemically Ordered Quaternary Atomically Laminated i-MAX Phases and Oxidation of $(Cr_{2/3}Y_{1/3})_2AlC$ and $(Mo_{2/3}Y_{1/3})_2AlC$. *J. Alloys Compd.* **2021**, *867*, 158930.
(29) Halim, J.; Etman, A. S.; Elsukova, A.; Polcik, P.; Palisaitis, J.; Barsoum, M. W.; Persson, P. O. Å.; Rosen, J. Tailored Synthesis Approach of $(Mo_{2/3}Y_{1/3})_2AlC$ i-MAX and Its Two-Dimensional Derivative Mo1.33CTz MXene: Enhancing the Yield, Quality, and Performance in Supercapacitor Applications. *Nanoscale* **2021**, *13* (1), 311−319.
(30) Zhao, N.; Chong, H.; Ma, Z.; Chen, Z.; Deng, W.; Lu, Y.; Qi, L.; Wang, Q.; Cui, W. Nanolaminated $(Mo_{1-X}M_x)_{4/3}Er_{2/3}GaC$ (M = Ti, V, Nb, Ta, W) i-MAX and 2D i-MXene Derivatives with Enhanced Supercapacitor Performance. *Ceram. Int.* **2024**, *50* (13), 22711−22721.
(31) Abbott, J.; Morris, V.; Adhikari, M.; Balabhadra, S.; Bretana, A.; Rai, B.; Autrey, D.; Gautam, B. Structural and Morphological Characteristics of Rare Earth Element-Based MAX Phase and MXene. *Microsc. Microanal.* **2024**, *30* (Suppl 1), 1215.
(32) Champagne, A.; Ricci, F.; Barbier, M.; Ouisse, T.; Magnin, D.; Ryelandt, S.; Pardoen, T.; Hautier, G.; Barsoum, M. W.; Charlier, J. C. Insights into the Elastic Properties of RE- i -MAX Phases and Their Potential Exfoliation into Two-Dimensional RE- i -MXenes. *Phys. Rev. Mater.* **2020**, *4* (1), 013604.
(33) Petruhins, A.; Lu, J.; Hultman, L.; Rosen, J. Synthesis of Atomically Layered and Chemically Ordered Rare-Earth (RE) i-MAX Phases; $(Mo_{2/3}RE_{1/3})_2GaC$ with RE = Gd, Tb, Dy, Ho, Er, Tm, Yb, and Lu. *Mater. Res. Lett.* **2019**, *7* (11), 446−452.
(34) Rai, B. K.; Mizzi, C. A.; Bretaña, A.; Breton, L.; Housley, C.; Ivy, D.; Abbott, J.; Maiorov, B.; Gautam, B. R.; Frontzek, M.; Rai, R. C.; Calder, S. Magnetic Properties of (Mo2/3Dy1/3)2AlC Arc Melted Polycrystalline Samples. *J. Magn. Magn. Mater.* **2025**, *624*, 172992.
(35) Tao, Q.; Lu, J.; Dahlqvist, M.; Mockute, A.; Calder, S.; Petruhins, A.; Meshkian, R.; Rivin, O.; Potashnikov, D.; Caspi, E. N.; Shaked, H.; Hoser, A.; Opagiste, C.; Galera, R. M.; Salikhov, R.; Wiedwald, U.; Ritter, C.; Wildes, A. R.; Johansson, B.; Hultman, L.; Farle, M.; Barsoum, M. W.; Rosen, J. Atomically Layered and Ordered Rare-Earth i-MAX Phases: A New Class of Magnetic Quaternary Compounds. *Chem. Mater.* **2019**, *31* (7), 2476−2485.
(36) Champagne, A.; Chaix-Pluchery, O.; Ouisse, T.; Pinek, D.; Gélard, I.; Jouffret, L.; Barbier, M.; Wilhelm, F.; Tao, Q.; Lu, J.; Rosen, J.; Barsoum, M. W.; Charlier, J. C. First-Order Raman Scattering of Rare-Earth Containing i -MAX Single Crystals $(Mo_{2/3}RE_{1/3})_2AlC$ (RE = Nd, Gd, Dy, Ho, Er). *Phys. Rev. Mater.* **2019**, *3* (5), 053609.
(37) Dahlqvist, M.; Rosen, J.; Tao, Q.; Zhou, J.; Palisaitis, J.; Persson, P. O. Å. Theoretical Prediction and Synthesis of a Family of Atomic Laminate Metal Borides with In-Plane Chemical Ordering. *J. Am. Chem. Soc.* **2020**, *142* (43), 18583−18591.
(38) Ghazaly, A. E.; Zheng, W.; Halim, J.; Tseng, E. N.; Persson, P. O.; Ahmed, B.; Rosen, J. Enhanced Supercapacitive Performance of Mo1.33C MXene Based Asymmetric Supercapacitors in Lithium Chloride Electrolyte. *Energy Storage Mater.* **2021**, *41*, 203−208.
(39) Meshkian, R.; Dahlqvist, M.; Lu, J.; Wickman, B.; Halim, J.; Thörnberg, J.; Tao, Q.; Li, S.; Intikhab, S.; Snyder, J.; Barsoum, M. W.; Yildizhan, M.; Palisaitis, J.; Hultman, L.; Persson, P. O. Å.; Rosen, J.; Meshkian, R.; Dahlqvist, M.; Lu, J.; Halim, J.; Thörnberg, J.; Tao, Q.; Yildizhan, M.; Palisaitis, J.; Hultman, L.; Å Persson, P. O.; Rosen, J.; Wickman, B.; Li, S.; Intikhab, S.; Snyder, J.; Barsoum, M. W. W-Based Atomic Laminates and Their 2D Derivative $W_{1.33}C$ MXene with Vacancy Ordering. *Adv. Mater.* **2018**, *30* (21), 1706409.
(40) Halim, J.; Palisaitis, J.; Lu, J.; Thörnberg, J.; Moon, E. J.; Precner, M.; Eklund, P.; Persson, P. O. A.; Barsoum, M. W.; Rosen, J. Synthesis of Two-Dimensional $Nb_{1.33}c$ (Mxene) with Randomly Distributed Vacancies by Etching of the Quaternary Solid Solution $(Nb_{2/3}Sc_{1/3})_2AlC$ Max Phase. *ACS Appl. Nano Mater.* **2018**, *1* (6), 2455−2460.
(41) Meshkian, R.; Lind, H.; Halim, J.; El Ghazaly, A.; Thörnberg, J.; Tao, Q.; Dahlqvist, M.; Palisaitis, J.; Persson, P. O. Å.; Rosen, J. Theoretical Analysis, Synthesis, and Characterization of 2D $W_{1.33}C$ (MXene) with Ordered Vacancies. *ACS Appl. Nano Mater.* **2019**, *2* (10), 6209−6219.
(42) Persson, I.; el Ghazaly, A.; Tao, Q.; Halim, J.; Kota, S.; Darakchieva, V.; Palisaitis, J.; Barsoum, M. W.; Rosen, J.; Persson, P. O. Å.; Persson, I.; el Ghazaly, A.; Tao, Q.; Halim, J.; Palisaitis, J.; Rosen, J.; Å Persson, P. O.; Kota, S.; Barsoum, M. W.; Darakchieva, V. Tailoring Structure, Composition, and Energy Storage Properties of MXenes from Selective Etching of In-Plane, Chemically Ordered MAX Phases. *Small* **2018**, *14* (17), 1703676.
(43) Yang, J.; Liu, R.; Jia, N.; Wu, K.; Fu, X.; Wang, Q.; Cui, W. Novel W-Based in-Plane Chemically Ordered $(W_{2/3}R_{1/3})_2AlC$ (R = Gd, Tb, Dy, Ho, Er, Tm and Lu) MAX Phases and Their 2D $W_{1.33}C$ MXene Derivatives. *Carbon* **2021**, *183*, 76−83.
(44) Yang, J.; Yao, G.; Sun, S.; Chen, Z.; Yuan, S.; Wu, K.; Fu, X.; Wang, Q.; Cui, W. Structural, Magnetic Properties of in-Plane Chemically Ordered $(Mo_{2/3}R_{1/3})_2AlC$ (R = Gd, Tb, Dy, Ho, Er and

https://doi.org/10.1021/acsanm.5c04789
ACS Appl. Nano Mater. 2026, 9, 1089−1098

Y) MAX Phase and Enhanced Capacitance of $Mo_{1.33}C$ MXene Derivatives. *Carbon* **2021**, *179*, 104−110.
(45) Chen, Z.; Chong, H.; Sun, S.; Yang, J.; Yao, G.; Wang, Q.; Zhu, J.; Yang, S.; Cui, W. Synthesis and Characterizations of Solid-Solution i-MAX Phase $(W_{1/3}Mo_{1/3}R_{1/3})_2AlC$ (R = Gd, Tb, Dy, Ho, Er and Y) and Derivated i-MXene with Improved Electrochemical Properties. *Scr. Mater.* **2022**, *213*, 114596.
(46) Ghazaly, A. E.; Méndez-Romero, U. A.; Halim, J.; Tseng, E. N.; Person, P. O. Å.; Ahmed, B.; Wang, E.; Rosen, J. Improved Charge Storage Performance of a Layered $Mo_{1.33}C$ MXene/MoS_2/Graphene Nanocomposite. *Nanoscale Adv.* **2021**, *3* (23), 6689−6695.
(47) Mostafaei, A.; Faizabadi, E.; Semiromi, E. H. Structural, Electronic and Optical Properties of Two-Dimensional $(M_{2/3}Y_{1/3})_2CO_2$ (M = Mo,W) IMXene. *Nanotechnol.* **2020**, *32* (1), 015703.
(48) Mostafaei, A.; Faizabadi, E.; Semiromi, E. H. Electronic Structures and Optical Properties of Two-Dimensional $(W_{2/3}X_{1/3})_2CO_2$ (X = SC,Y) IMXene by First-Principles Calculations. *Mater. Chem. Phys.* **2020**, *248*, 122896.
(49) Khazaei, M.; Wang, V.; Sevik, C.; Ranjbar, A.; Arai, M.; Yunoki, S. Electronic Structures of IMAX Phases and Their Two-Dimensional Derivatives: A Family of Piezoelectric Materials. *Phys. Rev. Mater.* **2018**, *2* (7), 074002.
(50) Makani, N. H.; Rai, B. K.; Bastakoti, B. P.; Bretana, A.; Gautam, B. Current Advances in I-MAX Phases and Their Two Dimensional Derivative i-MXenes: Challenges and Opportunities. *Adv. Electron. Mater.* **2025**, *11*, No. e00478.
(51) Kresse, G.; Hafner, J. *Ab Initio* Molecular Dynamics for Liquid Metals. *Phys. Rev. B* **1993**, *47* (1), 558.
(52) Kresse, G.; Furthmüller, J. Efficiency of Ab-Initio Total Energy Calculations for Metals and Semiconductors Using a Plane-Wave Basis Set. *Comput. Mater. Sci.* **1996**, *6* (1), 15−50.
(53) Blöchl, P. E. Projector Augmented-Wave Method. *Phys. Rev. B* **1994**, *50* (24), 17953.
(54) Kohn, W.; Sham, L. J. Self-Consistent Equations Including Exchange and Correlation Effects. *Phys. Rev.* **1965**, *140* (4A), A1133.
(55) Perdew, J. P.; Burke, K.; Ernzerhof, M. Generalized Gradient Approximation Made Simple. *Phys. Rev. Lett.* **1996**, *77* (18), 3865.
(56) Davidson, E. R. The Iterative Calculation of a Few of the Lowest Eigenvalues and Corresponding Eigenvectors of Large Real-Symmetric Matrices. *J. Comput. Phys.* **1975**, *17* (1), 87−94.
(57) Kakhidze, N.; Valikhov, V.; Selikhovkin, M.; Khrustalyov, A.; Zhukov, I.; Vasiliev, S.; Vorozhtsov, A. Effects of ErF_3 Particles on the Structure and Physicomechanical Properties of A359 Alloy. *Metals* **2023**, *13* (8), 1463.
(58) Petruhins, A.; Dahlqvist, M.; Lu, J.; Hultman, L.; Rosen, J. Theoretical Prediction and Experimental Verification of the Chemically Ordered Atomic-Laminate i-MAX Phases $(Cr_{2/3}Sc_{1/3})_2GaC$ and $(Mn_{2/3}Sc_{1/3})_2GaC$. *Cryst. Growth Des.* **2020**, *20* (1), 55−61.
(59) Teterin, Y. A.; Teterin, A. Yu. Structure of X-Ray Photoelectron Spectra of Lanthanide Compounds. *Russ. Chem. Rev.* **2002**, *71* (5), 347−381.
(60) Isacfranklin, M.; Yuvakkumar, R.; Ravi, G.; Hong, S. I.; Shini, F.; Thambidurai, M.; Dang, C.; Velauthapillai, D. Marigold Flower like Structured Cu_2NiSnS_4 Electrode for High Energy Asymmetric Solid State Supercapacitors. *Sci. Rep.* **2020**, *10* (1), 19198.
(61) Alonzo, S. M. M.; De, S.; Morris, V.; Autrey, D. E.; Gautam, B. R.; Pathiraja, G.; Bastakoti, B. P. Intercalation of Polyacrylonitrile Nanoparticles in $Ti_3C_2T_x$ MXene Layers for Improved Supercapacitance. *ACS Appl. Mater. Interfaces* **2024**, *16*, 64784−64796.
(62) Nashim, A.; Pany, S.; Parida, K. M. Systematic Investigation on the Charge Storage Behavior of $GdCrO_3$ in Aqueous Electrolyte. *J. Energy Storage* **2021**, *42*, 103145.
(63) Ardizzone, S.; Fregonara, G.; Trasatti, S. Inner" and "Outer" Active Surface of RuO_2 Electrodes. *Electrochim. Acta* **1990**, *35*, 263−267.
(64) BioLogic. ZFit and Equivalent Electrical Circuits. In *EC-Lab—Application Note #14*; Bio-Logic Science Instruments: Seyssinet-Pariset, 2009.
(65) BioLogic. Studying Batteries with Electrochemical Impedance Spectroscopy (EIS). In *White Paper #01*; Bio-Logic Science Instruments: Seyssinet-Pariset, 2017.
(66) Giovanelli, G.; Borghi, M.; Lodi, A.; Grasser, T.; Pasquali, L. Thin Epitaxial Ionic Fluoride Films for Electronics Applications. *Surfaces* **2025**, *8* (2), 22.

https://doi.org/10.1021/acsanm.5c04789
ACS Appl. Nano Mater. 2026, 9, 1089−1098